

Effect of molecular hydrogen self-shielding modeling on galaxy formation in cosmological simulation

THỊNH HỮU NGUYỄN^{1,2} AND KIRK S. S. BARROW¹

¹*Department of Astronomy, University of Illinois at Urbana-Champaign, Urbana, IL 61801, USA*

²*Center for AstroPhysical Surveys, National Center for Supercomputing Applications
Urbana, IL 61801, USA*

ABSTRACT

Modeling molecular hydrogen accurately is an important task in cosmological simulation because it affects star formation and galaxy evolution. Given the increasing capabilities of computational power in recent years, more robust and computationally-heavy techniques are now achievable. One of which is the use of ray tracing to model molecular hydrogen self-shielding. This paper evaluates the use of Sobolev-like approximation in self-shielding modeling - a method widely used to reduce computational cost in literature - and test whether it agrees with the results from a more vigorous ray tracing method. We run two high resolution zoom-in cosmological simulations with two models up to redshift of 10.9 to investigate their effects of galaxy evolution in the early universe. We find that the approximation model underestimates the level of H_2 self-shielding in low gas density environment, causing halos to lose a lot of H_2 when compared with the ray tracing model. The susceptibility of H_2 against high-energy radiation in the simulation with the approximation model prevents smaller halos from forming stars, while bigger halos seem to be uninfluenced by the choice of self-shielding model in terms of stellar mass. Within a halo, we show that the discrepancy between the approximation and the ray-tracing model is more prominent in the halo's outer region due to its low gas density. On a large scale, the approximation model have fewer metal-contaminated regions in the intergalactic medium, heats up the universe quicker, and speeds up the reionization process. These results show that the Sobolev-like approximation to model H_2 self-shielding alter various properties of galaxies and the large-scale universe, emphasizing a need for caution when employing this technique in running cosmological simulations.

Keywords: Astronomical simulations(1857) — Radiative transfer simulations(1967) — Galaxy formation(595) — Reionization(1383)

1. INTRODUCTION

Molecular hydrogen is a building block for star formation. For a gas cloud to collapse into a star, the cloud's self-gravity must be sufficiently large to overcome its pressure gradient. In the absence of other environmental effects, to achieve the collapse, the gas cloud usually needs to have sufficient mass or a high enough cooling rate so that the cooling time is smaller than the free-fall time. Since the cooling time generally decreases when the gas density increases during the collapse, this leads to catastrophic cooling and the gas pressure being lost against gravity, resulting in a collapse. Depending on the temperature and density, there are multiple radiative cooling mechanisms for a cloud to release its internal energy. For primordial gas clouds with atomic hydrogen HI being the dominant compo-

nent, Bremsstrahlung emission, atomic hydrogen's recombination, collisional ionization, and collisional excitation processes can help cool the gas down to at best the virial temperature of $10^4 K$, below which the cooling rate is too low (Thoul & Weinberg 1995). Elaborate in what condition (temperature, density) molecular hydrogen forms from atomic hydrogen. However, if molecular hydrogen H_2 is available, it can further stimulate cooling by opening up new cooling channels through its rotational and vibrational energy levels. This allows the gas to cool to ≈ 100 Kelvin degrees (Galli & Palla 1998), making it possible for the cloud to collapse into stars. This connection between star formation and H_2 can be reflected through the Kennicutt-Schmidt law (Schmidt 1959; Kennicutt 1998) and various observational evidence in nearby disk galaxies (Wong & Blitz 2002; Kennicutt et al. 2007; Leroy et al. 2013).

Ultraviolet (UV) radiation emitted by nearby active stars can photodissociate molecular hydrogen via the Solomon process (Solomon 1965 - private communication reported in Field et al. 1966, Stecher & Williams 1967). When absorbing a Lyman-Werner (LW) photon (11.2-13.6 eV), a molecular hydrogen molecule is excited from the ground state to an excited electronic state. Instead of radiatively decaying back to the bound state, about 15 percent of the molecules have their electrons decay into the vibrational continuum, which subsequently dissociates the molecule into atomic hydrogen. Dissociation rates through this mechanism can be inhibited through H_2 self-shielding, a phenomenon where the column density is large enough that the H_2 in the cloud's outer layer absorbs the LW radiation and hence shields the inner region. Previous studies point out the importance of including self-shielding in preserving the amount of molecular hydrogen required for star formation. When simulating a disc galaxy, (Christensen et al. 2012) notices an increase in the amount of cold gas and a clumpier interstellar medium when incorporating self-shielding in their simulation. Safranek-Shrader et al. (2017) finds that self-shielding is crucial in the development of H_2 in the disc's mid-plane, which accounts for 10-15 percent of the total gas mass. Therefore, the hydrogen self-shielding mechanism becomes pivotal in preserving the amount of molecular hydrogen and regulating star formation.

Through modeling a semi-infinite, static slab of gas irradiated on one surface, Draine & Bertoldi (1996) proposes an analytical expression to model H_2 self-shielding factor that includes the effect of **line overlap (do we need to elaborate this? also do we need to show the equation here)**. Maybe show all the papers that use this expression? Look at Hartwig+2015 for the list As shown in Equation (37) of Draine & Bertoldi (1996), the self-shielding factor is a function of the H_2 column density. In the past, computing the column density for multiple 3D directions was prohibitively computationally expensive (Shang et al. 2010; Wolcott-Green et al. 2011). Therefore, multiple methods have been suggested to approximate the self-shielding effect while trying to alleviate its demanding computational cost. A method is to define a local characteristic length scale across which the H_2 number density is constant. This characteristic length can be either the Jeans length (Shang et al. 2010; Johnson et al. 2011), the Sobolev length (Sobolev 1957; Yoshida et al. 2006), or the Sobolev-like length that is computed from the density-gradient (Gnedin et al. 2009; Gnedin & Kravtsov 2011). Rather than a single characteristic length, Hartwig et al. (2015a) approximates the 3D

column densities by creating spherical maps of the column density around each Voronoi cell with 48 equal-area pixels and also taking into account the Doppler effect from the relative velocities of the infalling gas particles. Another non-local method is the six-ray approximation (Yoshida et al. 2003, 2007; Glover & Mac Low 2007a,b), where the H_2 column density is integrated along six directions along three Cartesian axes centered at each particle's position.

However, there are limitations to the applicability of approximate treatments in various test problems when compared to the accurate full ray-tracing calculation. In the context of photodissociation of H_2 in protogalaxies and direct-collapse black hole formation, Wolcott-Green et al. (2011) show that the Sobolev length, the density gradient, and the six-ray approximation methods overestimate the H_2 shielding degree by an order of magnitude in low-density regions of $n < 10^4 cm^{-3}$. Also in the context of direct-collapse black hole, when comparing with their non-local approximation detailed in Hartwig et al. (2015a), Hartwig et al. (2015b) find that the Jeans approach returns a critical flux value J_{crit} - the lowest flux required for a halo with virial temperature above $10^4 K$ to collapse to a supermassive black hole seed - two times larger than the non-local approximation, leading to a disparity in the predicted number density of black hole seeds. Greif (2014) investigate the collapse of primordial star-forming clouds with an accurate H_2 line emission model and notice that the Sobolev method brings about a thermal instability for the collapsing cloud and an order-of-magnitude overestimation of the escape fraction for high optical depth. When evaluating the triggered Population III star formation at the limb of the HII region, Chiaki & Wise (2023) find that while the density-gradient method matches well with the ray-tracing method, the Jeans length approximation results in an overestimation of the number of the Population III stars at the front of the shock wave. The authors suggest that this is because the thickness of the H_2 ring of the shock front is typically smaller than the Jeans length, and thus the local approximation is inappropriate. In their large-scale galactic discs simulations, Safranek-Shrader et al. (2017) notices that the Sobolev method underpredicts the H_2 abundance in the disc by a factor of 5, while the six-ray and the Jeans length methods perform better, which is contrary to the findings that Jeans length method is ineffective in previous studies. Thus, the validity of these approximation methods is highly problem-dependent and they cannot be used as a general substitution for the full ray-tracing calculation.

163 A simulation that uses approximated H₂ self-
 164 shielding: COLDSIM, Maio et al 2021. Maybe
 165 mention that the Renaissance Simulation (and
 166 maybe others) doesn't implement self-shielding,
 167 so can affect the results.

168 In this paper, we expand the investigation by com-
 169 paring these approximation methods with the detailed
 170 ray-tracing methods, this time in the context of **star**
171 formation during the Reionization period. This
 172 will help further examine and inform the community
 173 about the applicability of these approximations in mod-
 174 eling H₂ in different contexts. In Section ..., we will
 175 describe our simulation and the implemented H₂ self-
 176 shielding models. Section ... analyzes the effect of these
 177 models on star formation and galaxy evolution during
 178 Reionization. Last but not least, in Section ..., we dis-
 179 cuss the implications of the findings and summarize the
 180 paper.

181
 182 *Maybe a paragraph at the beginning about the obser-*
183 vational and theoretical evidence of the relation between
184 H₂ and star formation (Kenicutt-Schmidt relation, for
185 example)? I think this is a good idea. I'm happy to
186 help with this part if you need some background.

2. METHOD

2.1. Cosmological simulations

187 We run and analyze outputs from a radiation-
 188 hydrodynamic adaptive mesh refinement simulation
 189 ENZO (Bryan et al. 2014). Two sets of cosmological
 190 simulations are generated to explore the self-shielding
 191 effect in the early stage and in the late stage of the
 192 Reionization period, which we will refer to as *Ear-*
193 lyRe and *LateRe*, respectively. In the early stage of
 194 Reionization, the UV background radiation is still lo-
 195 cal. Thus, the *EarlyRe* set provides a control sample
 196 to study whether the self-shielding approximation af-
 197 fects the overall star formation activity during a low
 198 non-local UV-radiation scenario. On the other hand,
 199 the *LateRe* allows us to study how the resistance of
 200 molecular clouds against a strong photoionization back-
 201 ground depends on the self-shielding treatments. Both
 202 sets assume a flat ΛCDM cosmology and are run with
 203 the cosmological parameters obtained from *Planck Col-*
204 laboration et al. (2016): $\Omega_M = 0.3065$, $\Omega_\Lambda = 0.6935$,
205 $\Omega_b = 0.0483$, $h = 0.679$, $\sigma_8 = 0.8154$, and $n = 0.9681$.
206 The total moving volume of the *EarlyRe* and *LateRe*
207 simulations are 13 (Mpc/h)³ and 5 (Mpc/h)³, respec-
208 tively. Both sets have the root grid dimension of 256³.
209 The total number of dark matter particles is $\approx 10^{7.82}$
210 particles for the *EarlyRe* set and $\approx 10^8$ particles for
211 the *LateRe* set. Inside the total volume of the *EarlyRe*

212 (*LateRe*) simulation, we create a smaller zoom-in region
 213 using three (**check the MUSIC file of LateRe**) ad-
 214 ditional levels of nested refinement to create an effec-
 215 tive grid size resolution of 2632.5 × 2512.9 × 2871.9 kpc³
 216 (920.5 × 1564.8 × 1196.6 comoving kpc³) at the last snap-
 217 shot at redshift of 10.9 (6.4). In the zoom-in region,
 218 the most refined dark matter particle mass is 2.7×10^4
 219 (1.5×10^3) M_\odot . As the density passes a certain thresh-
 220 old, the grids inside this zoom-in region can further be
 221 refined adaptively up to 2¹³ (2¹⁴) times the root grid
 222 dimensions. This allows a maximum spatial resolution
 223 down to 3.07 pc (1.89 pc) at the last time step, which
 224 allows the tracking of large molecular clouds through ini-
 225 tial collapse. We use radiative star cluster particle ([Wise & Cen 2009](#)) and Population III star particle ([Abel et al. 2007](#)) for our star formation prescription.

226 Each set contains a version running with detailed ray-
 227 tracing calculation (*EarlyRe-ray* and *LateRe-ray*) and a
 228 version running with a local approximation of the col-
 229 umn density (*EarlyRe-apx* and *LateRe-apx*) when com-
 230 puting the H₂ self-shielding factor. The self-shielding
 231 model is set by the *RadiativeTransferOpticallyThinH2*
 232 ENZO radiation parameter, where a value of 1 enables
 233 an optically thin H₂ dissociating Lyman-Werner radia-
 234 tion field and a value of 0 uses ray-tracing for the calcu-
 235 lation. For the *EarlyRe* simulation set, the *EarlyRe-ray*
 236 and the *EarlyRe-apx* are initialized with an identical list
 237 of parameters and initial conditions except for the *Ra-*
238 diativeTransferOpticallyThinH2 parameter. We evolve
 239 the two simulations from $z = 100$ to $z \approx 10.9$, each out-
 240 put is 1 Myr apart. For the *LateRe* set, to save com-
 241 putational time, we run the two simulations without
 242 ray-tracing until $z \approx 7.3$, then we switch the *Radi-*
243 aitiveTransferOpticallyThinH2 parameter to 0 for one of
 244 the simulations (the *LateRe-ray*) and run both of them
 245 until $z \approx 6.4$. This allows us to examine the effect of
 246 self-shielding near the end of the reionization epoch.

2.2. Halo tracking and merger tree algorithms

247 To identify the halos in the simulations, we employ
 248 SHINBAD (Barrow et al 2025, in preparation), an all-
 249 in-one algorithm that both finds halos and builds merger
 250 trees based on robust energy definition and particle
 251 tracking of dark matter particles. (**Note that this is**
 252 **version 1088 of SHINBAD, ask Kirk how to ex-**
253 pand this part). We exclude all the halos that are
 254 outside the refined region of the simulation box - the
 255 region containing only the highest and the second-most
 256 highest resolution dark matter particles - to ensure that
 257 the halos are physical.

2.3. Numerical H₂ self-shielding models

A H_2 self-shielding process happens when a molecular cloud has a sufficiently high column density that its outer layer absorbs all the Lyman-Werner UV photons, effectively shielding the molecules within it against photodissociation. Via modeling a semi-infinite, static slab of gas that is irradiated on one surface, [Draine & Bertoldi \(1996\)](#) express a self-shielding-accounted photodissociation rate as

$$k_{\text{diss}}(N_{H_2}, T) = f_{sh}(N_{H_2}, T) \cdot k_{\text{diss}}(N_{H_2} = 0, T), \quad (1)$$

where $f_{sh}(N_{H_2}, T)$ is a self-shielding factor or shielding function, and $k_{\text{diss}}(N_{H_2} = 0, T)$ is the dissociation rate in a optically-thin regime. At a low temperature (hundreds of K), the self-shielding factor can be approximately computed from only the H_2 column density,

$$f_{sh} = \min \left[1, \left(\frac{N_{H_2}}{10^{14} \text{cm}^{-2}} \right)^{-3/4} \right]. \quad (2)$$

This is controlled by setting the ENZO radiation parameter `RadiativeTransferH2ShieldType` = 0, which is also its default value. We use this expression to calculate the self-shielding factor in the EarlyRe-apx simulation. It is important to note that the convention of f_{sh} value is slightly counter-intuitive: the f_{sh} value of 0 means full self-shielding is available, and the f_{sh} value of 1 means there is no self-shielding. We also acknowledge that [Draine & Bertoldi \(1996\)](#) lists a more accurate formula to calculate f_{sh} that takes temperature as a parameter. However, using this formula does require additional computational resources that we save to run the ray-tracing scheme. Thus, we choose to use the approximated expression at low temperatures. **Check Gnedin and Draine 2014, where they do a comparison between this equation with a more accurate one (including line overlap).** Summarize their results here.

Maybe talking about the limitations of Draine and Bertoldi 1996, as on page 5, right column of Wolcott-Green.

To avoid the high computational expense of finding the H_2 column density in multiple 3D directions, previous studies employ different techniques to approximate it (see Section 1). In this paper, we compare the results from two methods: a direct integration from ray tracing and a Sobolev-like length approximation ([Gnedin et al. 2009; Wolcott-Green et al. 2011](#)). Even though demanding more computational time, the ray tracing treatment ensures a more accurate radiative transfer calculation. ENZO uses the adaptive ray tracing technique ([Wise & Abel 2011](#)) that is based on the HEALPix (Hierarchical Equal Area isoLatitude Pixelation, [Gorski et al.](#)

205) scheme. The column density is integrated along a
206 HEALPix rays,

$$N_{H_2} = \int n(H_2) ds. \quad (3)$$

215 The Sobolev-like treatment is a local approximation
216 in which the number density n_{H_2} is assumed to be con-
217 stant within a characteristic length scale L_{char} . In the
218 Sobolev-like approximation, the characteristic length
219 scale is defined as a distance over which the cell's gas
220 density ρ diminishes. The gas beyond this distance is
221 sparse enough that its influence on shielding is negli-
222 gible, and thus molecular hydrogen is dissociated in an
223 optically thin fashion. The column density is then com-
224 puted by

$$N_{H_2} \approx n_{H_2} L_{\text{char}} = n_{H_2} \frac{\rho}{|\nabla \rho|} \quad (4)$$

256 The approximation is enabled by setting the ENZO
257 parameters `RadiativeTransferOpticallyThinH2` = 1
258 and `RadiationShield` = 2.

259 Figure 1 compares the self-shielding factor f_{sh} be-
260 tween the ray-tracing model and the Sobolev-like ap-
261 proximation model. At the time step corresponding to z
262 = 10.9, we select 31 halos that contain stars or overlap
263 with another halo that contains stars. For each halo, we
264 select two gas cells to evaluate the self-shielding factor:
265 (1) the gas cell with the highest gas density, and (2)
266 the gas cell with the highest gas density gradient. Each
267 scatter point in Figure 1 represents a selected gas cell.
268 In the approximation model, the self-shielding factor of
269 a gas cell is calculated using Equations 2 and 3. For the
270 ray-tracing model, since the simulation output does not
271 store the photodissociation rate calculation, we need to
272 re-compute the self-shielding factor using Equation 2 with
273 an attenuated LW flux-weighted average column den-
274 sity. The LW flux from each star to a selected gas cell
275 is calculated as follows. Firstly, the intrinsic spectrum
276 of a star particle is generated using the Flexible Stellar
277 Population Synthesis (fsps) with the age and metallicity
278 of the star particle as inputs. We assume an initial mass
279 function from [Davé \(2008\)](#) evaluated at $z = 0$, and we
280 use the MIST isochrone library and MILES spectral li-
281 brary to generate the spectra. **may cite Susie's paper**
282 **here or ask her for more information.** Then, we
283 calculate the attenuation by including both scattering
284 and absorption due to H/He and metals **Ask Kirk to**
285 **include how the absorption and scatterings are**
286 **computed.** With the scattering and absorption coeffi-
287 cients, we can compute the total optical depth and then
288 the attenuation of the stellar spectrum from the source
289 to the target gas cell. Lastly, we calculate the attenu-
290 ated flux of each source to the gas cell, compute the LW

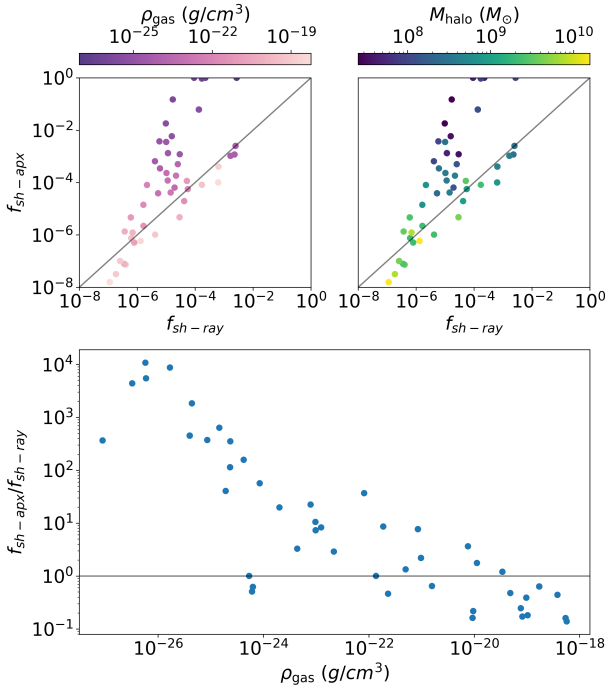


Figure 1. The comparison between the self-shielding factor between the *EarlyRe-ray* and the *EarlyRe-apx* simulation, evaluated at $z = 10.9$. Two gas cells with the highest gas density and highest gas density gradients are chosen in 31 halos in different mass range to evaluate the self-shielding factors. (Top) The relationship between the self-shielding factors calculated by the Sobolev-like approximation model and the ray-tracing model, colored by the cell’s gas density (top left) and the host halo’s mass (top right). (Bottom) The ratio between the approximated and the ray-traced self-shielding factors is plotted as a function of gas density. The Sobolev-like approximation tends to overestimate the amount of H_2 self-shielding in the high gas density regime and underestimate it in the low gas density regime.

flux-weighted average H_2 column density, and get the self-shielding factor from the ray-tracing model. It is important to note that we only include stars within the halo’s virial radius to estimate the flux-weighted average H_2 density because stars outside the radius are too far from the selected gas cell to contribute considerably to the total flux at the selected gas cell.

Figure 1 demonstrates a clear disparity in the f_{sh} value between EarlyRe-apx and EarlyRe-ray. In particular, the approximation model tends to overestimate the amount of shielding for cells with a gas density larger than $10^{-20} g/cm^3$ by up to 1 dex. On the other hand, diffuse gas is subjected to underestimated H_2 self-shielding when the Sobolev-like approximation model is used. For highly diffuse gas, this underestimation can be up to 3–4 dex. This connection between gas density and f_{sh} implies a mass-dependent effect of the self-shielding ap-

proximation model on halos. The top right subfigure of Figure 1 shows that larger halos ($M_{halo} > 10^{9.5} M_\odot$) have their molecular cloud region over-shielded in the approximation model because the gas is denser. On the other hand, the molecular clouds in small halos ($M_{halo} < 10^{8.5} M_\odot$) are under-shielded against LW radiation when using the Sobolev-like approximation. In some cases, the approximation returns no shielding effect even though those gas cells are still weakly shielded ($f_{sh} \approx 10^{-3}$ when ray-tracing is utilized). Only molecular gas clouds in halos whose mass is about $10^9 M_\odot$ are well modeled in the approximation model. The significance of this effect on star formation will be explored in Section 3.1.

Maybe a comparison in terms of the time run between the two methods

2.4. Cross-matching halos

To examine how each individual halo is affected by the implementation scheme of H_2 self-shielding, we perform cross-matching between halos in the simulations with ray-tracing and their counterparts in the simulations with the Sobolev-like approximation. The matching requirements are

$$\frac{2}{3} < \frac{M_{vir_{ray}}}{M_{vir_{apx}}} < \frac{3}{2} \quad (5)$$

$$\frac{d_{COM}}{R_{vir_{ray}}} < 0.5, \quad \frac{d_{COM}}{R_{vir_{apx}}} < 0.5$$

If there are multiple halos matching to one halo, we select the pair with lowest $\frac{d_{COM}}{R_{vir}}$ value. The virial mass and radius in Equation 5 come from SHINBAD and are calculated using only dark matter. We cross-match all the halos at the last timestep of the simulations and then trace back their merger tree (details in Subsection 2.2).

2.5. Star assignment

We uniquely assign each star particle in the simulation to one dark matter halo in a two-step fashion. For the first step, a star particle is assigned to a halo where it is first created. If a star particle is created inside the intersection of multiple halos, we will calculate the orbital energy of that star particle with respect to each halo’s center to determine which halo the particle belongs to. The assigned halo is the one with lower relative total orbital energy. We assume that a star particle never leaves its assigned halo unless that halo merges with another one, in which case the star particle will become a member of the descendant halo of the merger. This assumption allows a quick assignment of stars to halos without the need to calculate the orbital energy of each

star to multiple halos, which is computationally expensive. The assignment's first step starts from the first snapshot to the last snapshot of the simulation.

Even though stars do not generally leave a halo's potential well for isolated halos, the behavior becomes more complex during halo-halo interaction as stripping can occur and stars can be lost from one halo to another (Kannan et al. 2015). Therefore, the second step of our process is to address this shortcoming of the first step's assumption and to refine the star assignment result. In this step, we validate the output from the first step and check whether a star remains in its assigned halo's virial radius throughout its lifetime. If a star escapes the virial radius of its originally assigned halo, we assign that star to a new halo under two conditions: (1) the star's position must be within the new halo's virial radius and (2) the star's total orbital energy with respect to the new halo must be negative. Similar to the first step, if a star is located inside multiple potential new halos, we assign that star to the halo with the lowest negative orbital energy. If either Condition (1) or (2) fails at a certain timestep, this suggests that the star is stripped out of the potential well of all halos and thus we remove that star from the halo assignment process of that time step.

Once each star particle is uniquely associated with one halo, we calculate a halo's stellar mass and SFR exclusively based on its member star particles. This gravitational unbinding of star particles guarantees that each halo's stellar mass profile are not overlap and independent of each other.

2.6. Defining ISM, CGM, and IGM

The boundary of the interstellar medium (ISM), the circumgalactic medium (CGM), and the intergalactic medium (IGM) region in our analysis is defined as follows. The ISM region (or the boundary of a galaxy) starts from the galaxy's center of mass to $R_{\text{bary},2000}$, which is the radius enclosing a baryonic (gas and stars) mass density 2000 times the universe's critical mass density at a certain redshift. Even though there are multiple other definition of the boundary of galaxy in literature, such as using a fixed fraction of the virial radius, a fixed physical radius, or a radius that is scaled with mass or surface brightness (see Stevens et al. 2014 for a summary of these techniques), our over-density approach helps define the galaxy more robustly and more physically because it is redshift and density dependent. It also helps better define the galaxy during a close galaxy interaction when a half-mass radius or half-light radius approach may fail as another galaxy is in the target galaxy's virial radius. Depending on the redshift and the galaxy's compactness, $R_{\text{bary},2000}$ typically ranges from

0.15 to 0.25 times the halo's virial radius, which falls in the same range as other galaxy's aperture definitions in cosmological simulations (Stevens et al. 2014). The CGM starts from $R_{\text{bary},2000}$ to $R_{\text{halo,vir}}$, and the IGM is the region outside of the virial radius of all halos.

Also, it is important to note that the baryonic center of mass does not always coincide with the halo's center of mass. Thus, in some cases, we shift the virial region to be centered on the gas and stellar mass instead of the dark matter mass; however, this shift is not large and does not affect our interpretation.

3. RESULTS

3.1. Effect on the molecular hydrogen content and star formation

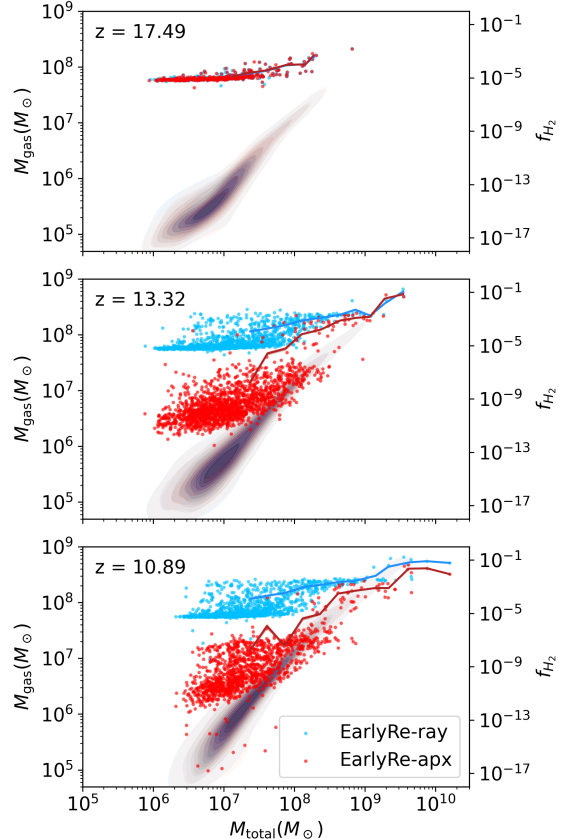


Figure 2. The relationship between the H_2 fraction and the total mass in the timestep where stars first appear, in the intermediate, and in the last timestep of the *EarlyRe* dataset. The contour plots show the M_{gas} distribution and the scatter points show the H_2 fraction of all halos in the simulation box.

Because the column density approximation model directly concerns the calculation of the molecular hydrogen density, we first investigate the amount of H_2 in

the ray tracing and approximation treatment. Figure 2 shows the H_2 fraction (f_{H_2}), which is the ratio between the H_2 mass with the total gas mass, as a function of the total halo mass in three snapshots, one at the time where star particles first appear in the simulations ($z \approx 17.49$), one at the time step in the middle of the simulation run ($z \approx 13.32$), and one being the last time step of the run ($z \approx 10.9$). Each halo in the snapshot is represented by a scatter point, the line represents the running average of each total mass bin, and the shaded region around the line is the standard deviation of the scatter points within each mass bin. The contour plots represent the distribution of the halos in the $M_{\text{gas}} - M_{\text{total}}$ space. According to Figure 2, both EarlyRe-ray and Early-apx simulations have similar gas mass distribution across all timesteps, showing f_{H_2} represents the amount of H_2 in the halos. However, f_{H_2} shows a notable difference between the two radiative transfer treatments, especially at the later time step and in the lower-halo-mass regime. For halo mass smaller than $10^8 M_\odot$, the f_{H_2} in the ray-tracing treatment is larger than that of the Sobolev-like approximation treatment by 3 to 6 dex. This difference grows larger as the simulation evolves, reaching up to 12 dex at the last time step for small halos. The EarlyRe-ray simulation also develops a lower limit for f_{H_2} of around 10^{-5} , whereas the f_{H_2} is allowed to reach much further value in the EarlyRe-apx simulation. This shows that the ray-tracing treatment models the self-shielding effect much better and thus helps preserve more molecular hydrogen in the halos. As pointed out in Figure 1, the approximation treatment considerably underestimates H_2 self-shielding in a low gas density regime and molecular hydrogen to get photodissociated more easily, inferring that smaller halos are the most susceptible to the choice of the model. At a higher mass range, the difference in f_{H_2} between the two models gradually diminishes. This is reasonable because larger halos have deeper gravitational potential well and have more dense cool gas regions where H_2 exists. In these regions, the approximation model matches well with the ray-tracing model (as shown in Figure 1), leading to an agreement of f_{H_2} between the two runs.

We proceed to investigate whether the self-shielding treatment affects the stellar mass of galaxies in the simulation. Figure 3 shows the relationship between stellar mass and halo mass between the *Early-Ray* and *Early-apx* in the time step where stars first appear (top left panel), in the last time step of the dataset (bottom right panel), and in the intermediate time steps. Figure 4 displays the number of halos that host stars as a function of time for different halo mass bins. The stellar component of the halos is unbound by using the star

assignment procedure described in Section 2.5. Even though the number of halos with stars is even between *EarlyRe-apx* and *EarlyRe-ray* in the beginning, there are more halos with stars in *EarlyRe-ray* at the end of the simulation, particularly halos with $M_{\text{halo}} < 10^9 M_\odot$. For ease of reference and lack of a better term, we will use the term "galaxy" to refer to a halo with stars, as opposed with halos with only gas and dark matter particles. From 375 million years after the Big Bang to near the end of the simulation ($z \approx 11.88 - 11$), there are two to four galaxies more in the simulation with the ray-tracing treatment. Furthermore, at a similar halo mass, smaller halos in *EarlyRe-ray* tend to have more stars than their counterparts in *EarlyRe-ray* by several dex in solar mass. This indicates that the use of Sobolev-like approximation for H_2 self-shielding treatment inhibits star formation activity in small halos and dwarf galaxies. On the other hand, halos whose dark matter mass is larger than $10^9 M_\odot$ show good agreement in stellar mass, suggesting that the stellar components of large halos are unaffected by our choice of H_2 self-shielding model. This observation aligns with Figure 2, where we see that H_2 is more accurately shielded in higher halo mass in *EarlyRe-apx*.

Another difference between *EarlyRe-ray* and *EarlyRe-apx* is the time when star particles first appear in the simulation. According to Figure 4, the formation of the first galaxy in *EarlyRe-apx* occurs 16 million years before that in *EarlyRe-ray*. The first galaxies in the two simulations both form in a halo with a dark matter mass smaller than $10^9 M_\odot$. This is rather intuitive, given that previous evidence shows that for small halos, stars form easier in the simulation using a ray-tracing model. However, further investigation suggests that the timing discrepancy in the formation of first stars is likely due to a stochastic nature of our star formation prescription rather than a physical reason. Before the first stars appear in a halo in *EarlyRe-apx*, the temperature and density distribution of gas and molecular hydrogen of the counterpart halo in *EarlyRe-ray* are similar to the halo in *EarlyRe-apx*. More discussion and plots regarding the first galaxies in the two simulation will be directed to the Appendix. **Reminder to include the appendix**

3.2. Case study on star formation

In this section, we analyze the properties of two halos, one being the largest halo in the simulation and one having a halo mass of $\approx 1.7 \times 10^9 M_\odot$, which is in the mass range where the approximation in H_2 self-shielding fails to accurately model star formation, as suggested in Figure 3. We match the halos between *EarlyRe-ray* and *EarlyRe-apx* using the procedure in Section 2.4. These

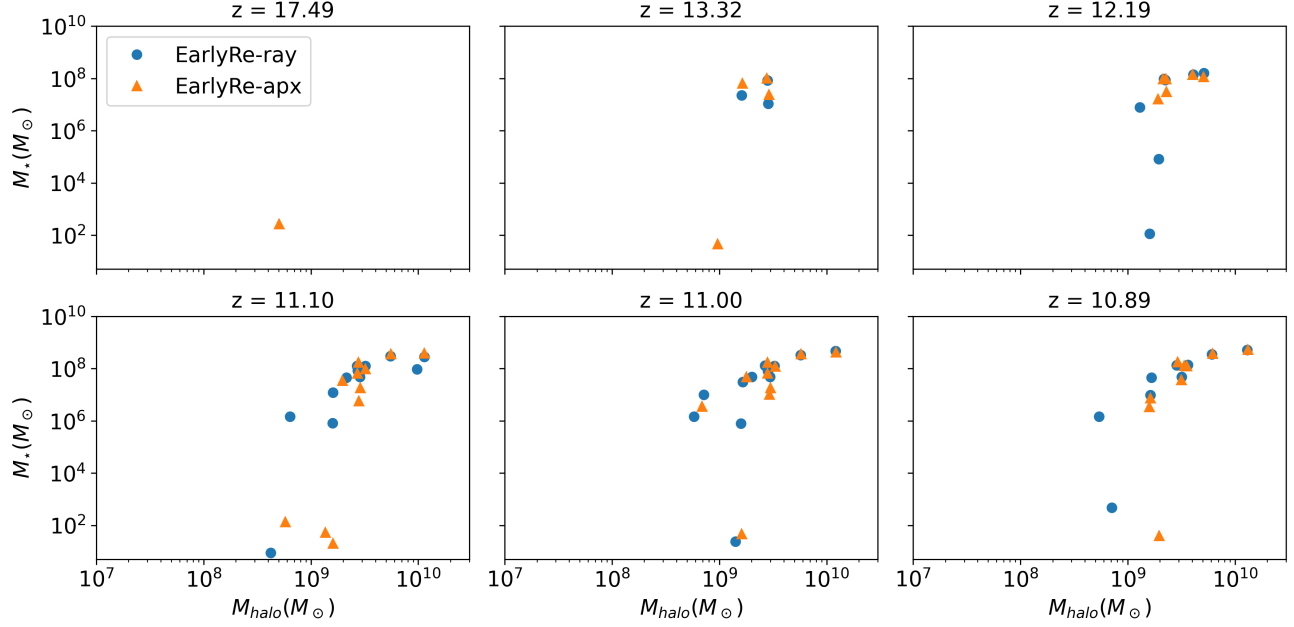


Figure 3. The relationships between stellar mass and total mass of all the halos in the timestep where stars first appear, in the intermediate timesteps, and in the last timestep of the *EarlyRe* dataset.

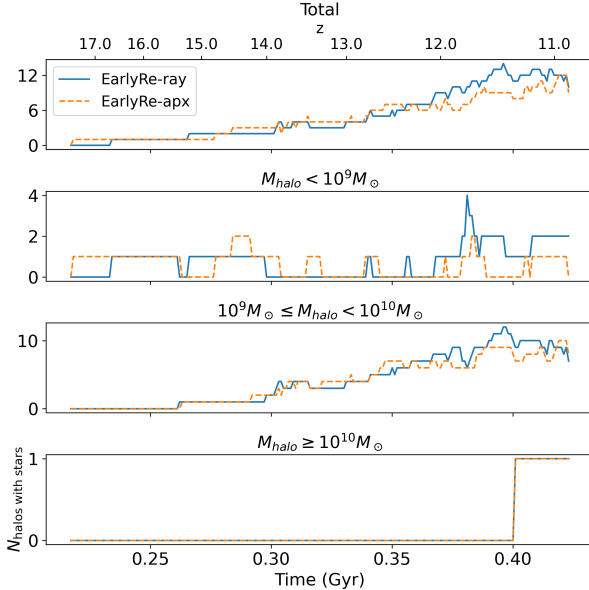


Figure 4. The comparison of the number of halos with stars as a function of time for each halo mass bin between the *EarlyRe-ray* and the *EarlyRe-apx* simulations.

two pairs of halos serve as examples to how the H_2 self-shielding modeling affects the galaxy properties.

Figures 5 and 6 show the projection of various properties at the last time step and the time evolution of those properties for the two halos in our case study. As hinted earlier by Figure 2, gas mass stays consistent between *EarlyRe-apx* and *EarlyRe-ray* throughout the halo's evolution and thus is unaffected by the choice of

H_2 self-shielding modeling. The gas density projection plot also looks relatively similar between our two runs. However, even though there is an agreement on total gas content, the amount of H_2 is considerably different in two simulations. For the largest halo, the mass of H_2 starts to diverge around $z \approx 14$, and *EarlyRe-ray* has about 10 times more H_2 in that halo than *EarlyRe-apx*. For the smaller halo, the discrepancy in the H_2 content is much more severe. Early in the simulation, the ray-tracing model consistently returns about 0.5 dex more mass than the approximation model. At $z \approx 11.5$, while *EarlyRe-ray* witnesses a quick rise in molecular gas, *EarlyRe-apx* maintains the same level of H_2 , intensifying the difference to be up to 2 dex in M_{H_2} between the two simulations at the last snapshot. This difference in H_2 matches our observation in Figure 2. In addition to H_2 mass, the distribution of molecular hydrogen is also different. In both halos that we use as examples, molecular hydrogen exists in clumps of high density ($\approx 10^{-21} \text{ g/cm}^3$) with respect to the surrounding. These clumps are located inside the galaxy (indicated by the white circle in the figures) and are concentrated in the galactic center. Outside of these clumps, H_2 gas density is quite low, reaching down to 10^{-36} g/cm^3 , proving that H_2 is completely photo-dissociated. In contrast, the halos in the *EarlyRe-ray* set displays a much more uniform distribution of molecular hydrogen. While H_2 density is still highest at the halo's center, H_2 density in the surrounding region is only 2-3 dex lower, showing that H_2 is able to exist and form in the outer part

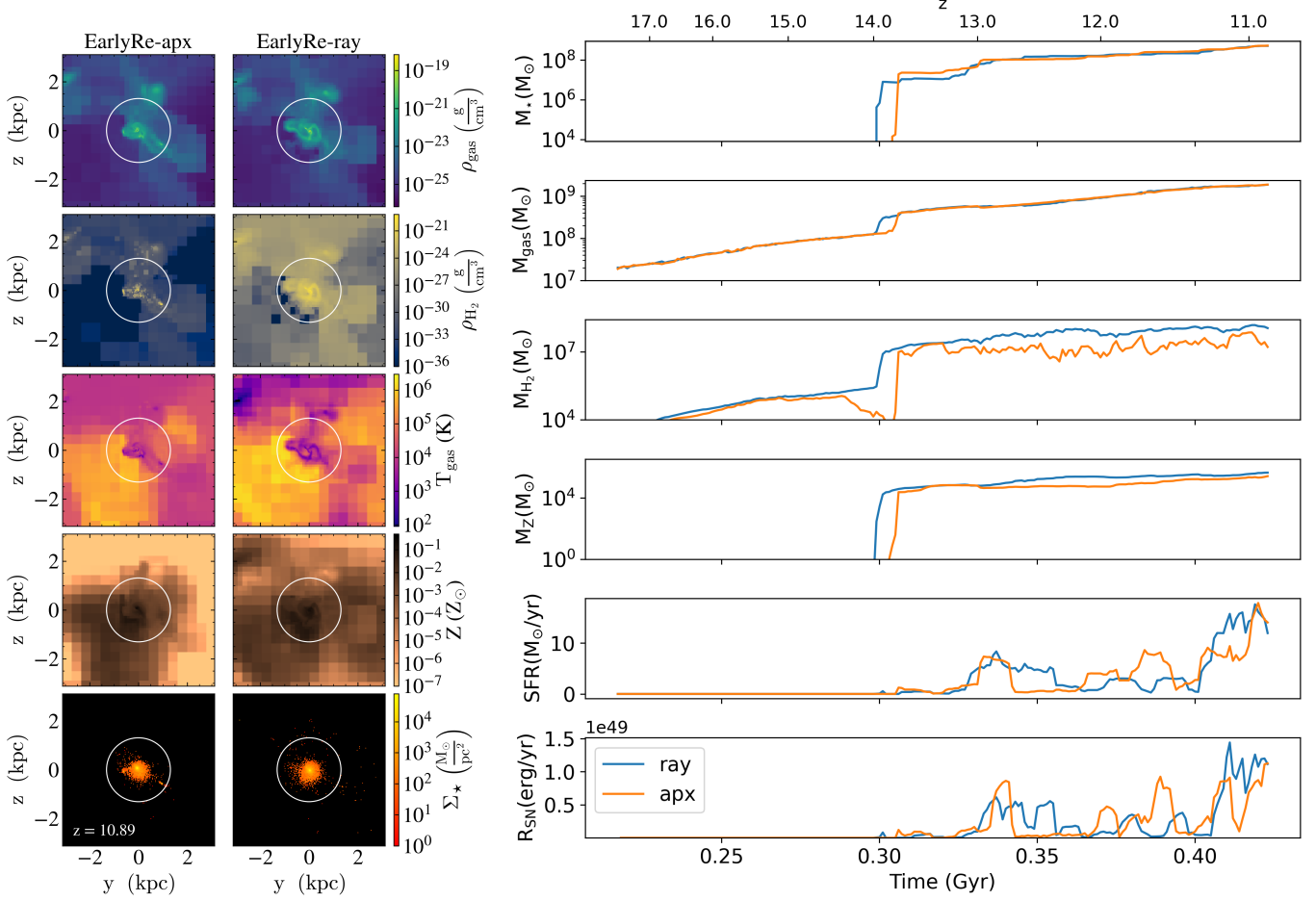


Figure 5. (Left) The gas density, H_2 density, temperature, metallicity, and stellar surface density projection plot of Halo 0 ($M_{\text{halo}} \approx 1.3 \times 10^{10} M_{\odot}$ at $z = 10.89$) within one virial radius. The white circle represents the boundary of the galaxy, which is defined as the radius enclosing the baryonic density 2000 times larger than the critical density of the universe. (Right) The time evolution of different properties in Halo 0 between the *EarlyRe-ray* and *EarlyRe-apx* simulations.

of the galaxy and even in the CGM. Indeed, the existence of H_2 outside the galactic center is what causes the discrepancy in the H_2 fraction between *EarlyRe-apx* and *EarlyRe-ray*. More details on the topic of ISM and CGM will be discussed in Section 3.3.

With regards to stellar mass, the different in self-shielding modeling results in greater differences in smaller halos than in bigger halos, as pointed out in Figure 3. For the case of the biggest halo in the simulation, Figure 5 shows that the stellar mass of the halo converge after $z \approx 13$, even though *EarlyRe-ray* forms its first stellar particles a few million years earlier. On the other hand, for the smaller halo in Figure 6, the halo modeled with ray-tracing forms stars approximately 20 million years prior to the *EarlyRe-apx*'s counterpart. Furthermore, throughout most of this halo's evolution, the stellar mass in *EarlyRe-ray* stays about several dex higher

in the *EarlyRe-apx* version and relatively converge at the last snapshot. Thus, this shows that the choice of H_2 self-shielding model affects the timing of star formation in halos while the stellar mass between two models will eventually converge.

In addition to the difference in stellar mass, the star formation history shows that the halo in the ray-tracing model experience more prolonged period of star formation while the halo in the approximation model experience shorter but stronger star formation episode (more detailed explanation maybe?). This behavior also happens in other large halos in the simulation box (for brevity purpose, they are not shown in the paper). The prolonged star formation period leads to prolonged supernova rate, thus affecting the metal mixing and metal distribution of the galaxy. As supernovas go off in longer time period, more metals are produced at once

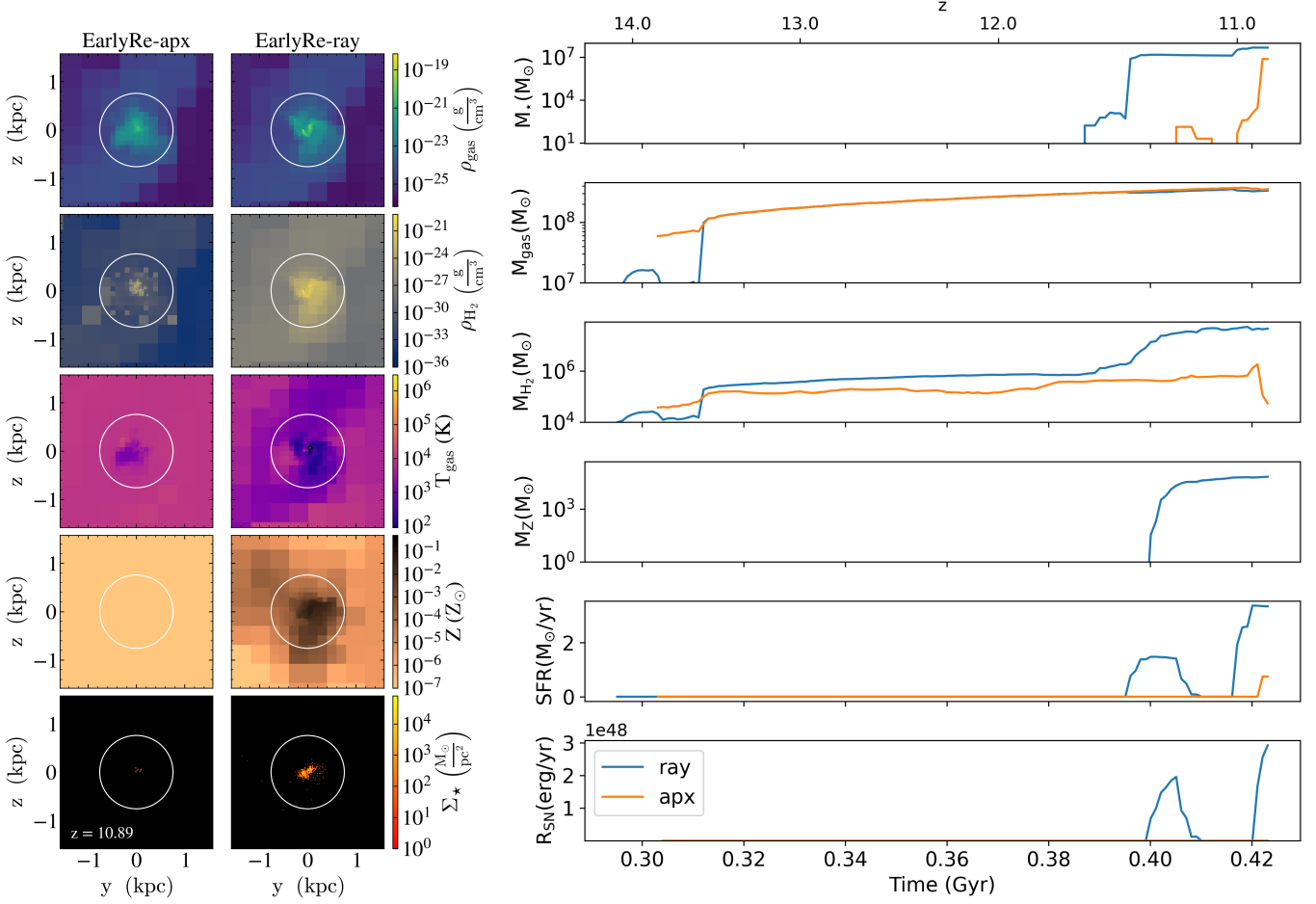


Figure 6. Same as Figure 5, but for another halo whose $M_{\text{halo}} \approx 1.7 \times 10^9 M_{\odot}$ at $z = 10.89$.

and thus it takes a longer time for the metals to mixed with the surrounding gas. This leads to what we see in the metallicity projection plot, where metals are less mixed and more uniformly distributed in the *EarlyRe-ray* set. More metals also results in more efficient cooling of gas, which is reflected in the temperature projection plot. These behaviors are more prominent in smaller halos, showing again that smaller halos are more susceptible by H_2 self-shielding modeling than of bigger halos.

3.3. Effect on the galaxy and CGM

In this section, we more closely examine the effect of H_2 self-shielding modeling on the ISM, the CGM, and the IGM to help further explain the previous observations we have on star formation.

Following the two case studies we examined in Section 3.2, Figures 7 and 8 show the gas and H_2 phase plot of the largest halo in the simulation ($M_{\text{halo}} = 1.3 \times 10^{10} M_{\odot}$) and a smaller halo of mass $M_{\text{halo}} \approx 1.7 \times$

$10^9 M_{\odot}$. The plots are separated into the galaxy (top row) region and the CGM region (bottom row). One noticeable disparity between *EarlyRe-ray* and *EarlyRe-apx* is the inefficiency of the gas to cool down below $10^4 K$ due to the lack of molecular hydrogen in the region. With atomic hydrogen HI being the only dominant component, processes such as Bremsstrahlung emission, atomic hydrogen's ionization and excitation processes can only help cool the gas down to $10^4 K$, while the existence of H_2 can introduce more energy levels to lower gas temperature. Thus, we can see a high concentration of gas at $10^4 K$ at low to intermediate density ($\rho_{\text{gas}} \leq 10^{-22} \text{ g/cm}^3$) when using the approximation model. The gas in *EarlyRe-apx* can only cool down to lower temperature after reaching a density of $\approx 10^{-22} \text{ g/cm}^3$ - the limit which the approximation model can better predict the H_2 self-shielding factor, according to Figure 1. When the gas is dense enough, the self-shielding of H_2 is approximated by *EarlyRe-apx* more accurately, leading to more H_2 to exist and

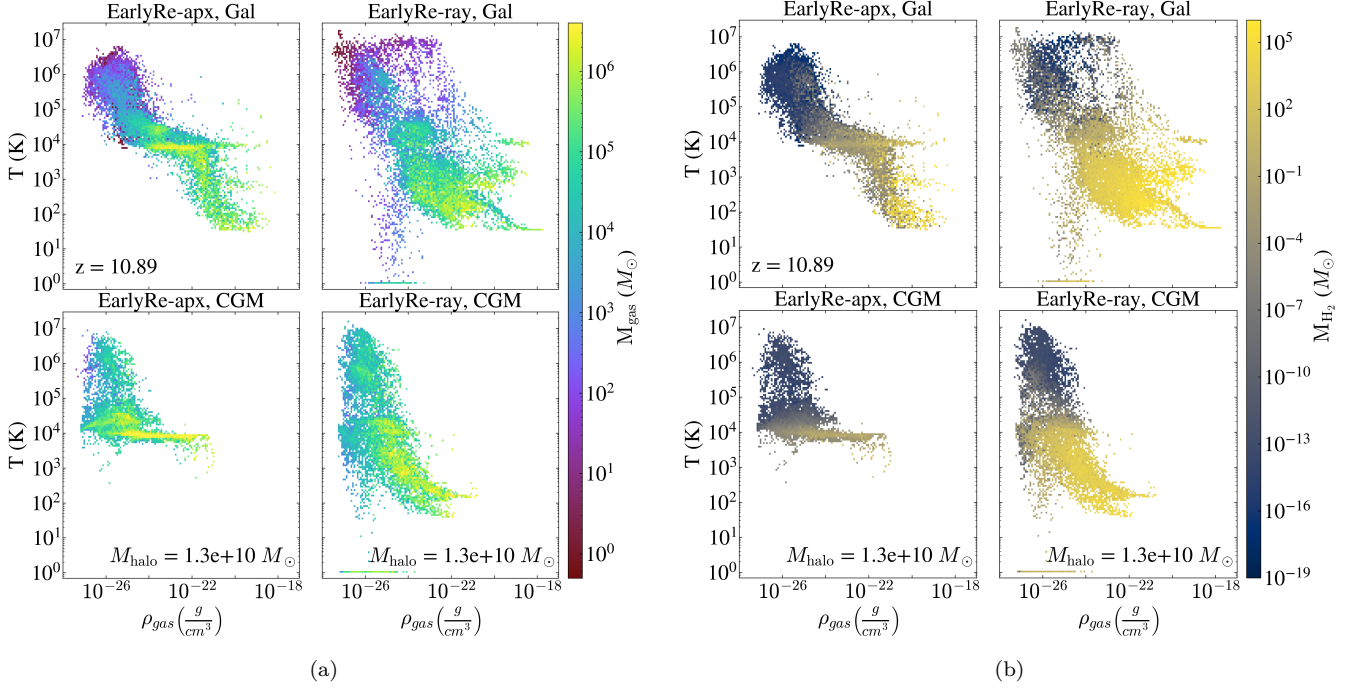


Figure 7. The gas phase plot colored by gas mass (Sub-figure (a)) and by molecular hydrogen mass (Sub-figure (b)) of the largest halo ($M_{\text{halo}} = 1.3 \times 10^{10} M_{\odot}$) in our simulation set, evaluated at the last time step $z = 10.89$. For each sub-figure, the left column shows the halo in *EarlyRe-apx*, and the right column shows its counterpart in *EarlyRe-ray*. The top row in each subfigure shows the phase plot using the gas cells within the galaxy region ($r \leq R_{\text{bary},2000}$), and the bottom row shows the phase plot using the gas cells in the CGM region ($R_{\text{bary},2000} < r \leq R_{\text{vir}}$).

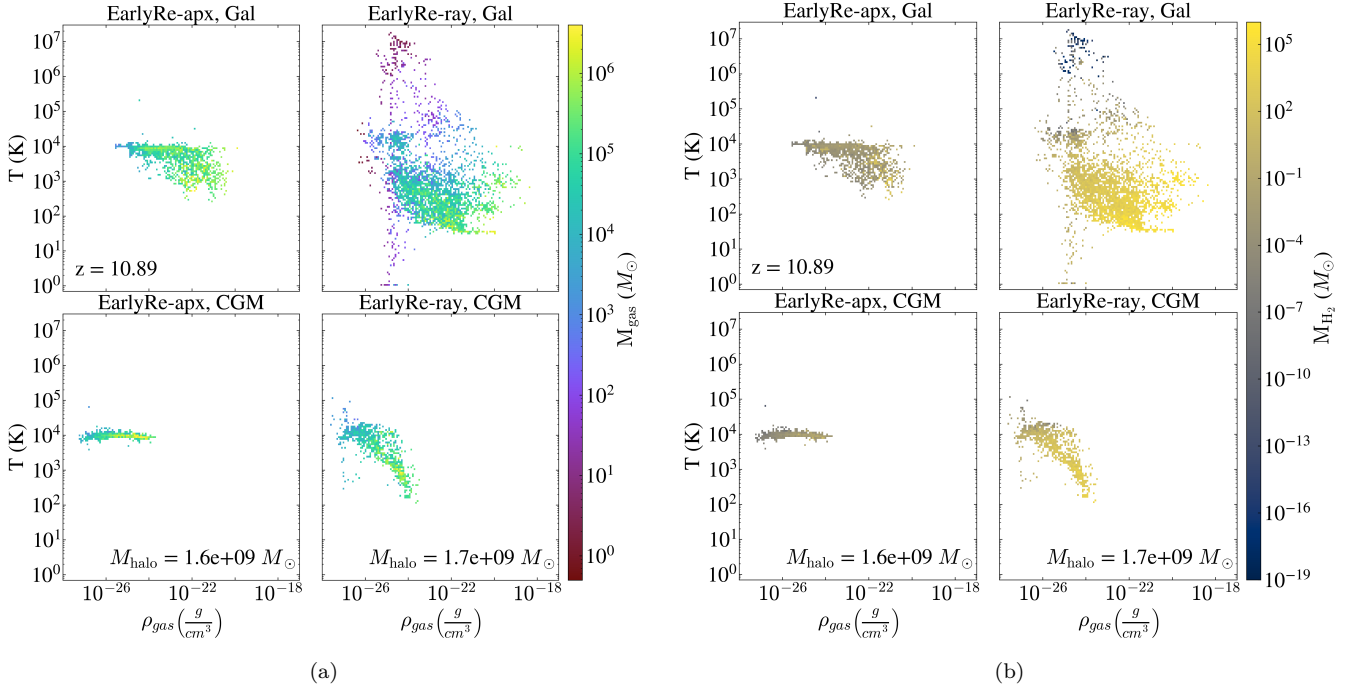


Figure 8. Similar to Figure 7, for a halo with mass $M_{\text{halo}} \approx 1.7 \times 10^9 M_{\odot}$ at $z = 10.89$.

gas to cool down. Indeed, according to the H_2 phase plot, H_2 exists most abundantly at the gas density of $\rho_{H_2} \geq 10^{-22} \text{ g/cm}^3$. The phase plot also re-affirm that the amount of H_2 existed in the *EarlyRe-apx*'s galaxy is much smaller than that of *EarlyRe-ray*, as pointed out in Figure 5. On the other hand, the large amount of molecular hydrogen in *EarlyRe-ray* existing even at low density helps cool down more of the gas. This allows gas to become denser. For example, the densest gas cell in the *EarlyRe-ray*'s galaxy in Figure 7 reaches the density above 10^{-18} g/cm^3 , about 10 to 100 times higher than the densest region in the *EarlyRe-apx*'s galaxy. It is important to note that for the radiative star cluster model and the Population III star model used in our simulation, their overdensity thresholds for a star particle to form are 10^7 and 10^6 , respectively. At the last time step ($z = 10.89$), these overdensity thresholds correspond to a gas density threshold of 4.5×10^{-20} and 4.5×10^{-21} . This suggests that both *EarlyRe-ray* and *EarlyRe-apx* galaxies are able to form stars; however, since *EarlyRe-ray* has more denser gas cells, it can form stars easier and quicker. **(so why the two stellar mass is the same?)** Furthermore, this effect is more prominent for lower halo. When using the approximation model, the gas within the *EarlyRe-apx*'s galaxy shown in Figure 8 cannot cool down below $10^3 K$ or gets denser than 10^{-20} g/cm^3 , while its counterpart can reach below $10^2 K$ and about 10^{-18} g/cm^3 thanks to much more H_2 being available.

In the CGM, gas has lower density and thus H_2 is more susceptible to destruction by LW radiation when using the approximation model. For both halos in our case studies, there is very little H_2 existing in the CGM in the *EarlyRe-apx* simulation. This keeps the gas in the CGM relatively hot at the minimum of $10^4 K$. In contrast, for *EarlyRe-ray* simulation, H_2 still exists in sufficient quantity outside of the galaxies that the CGM gas can cool down to a few hundred kelvins. Therefore, the use of the self-shielding model significantly effect the temperature and density profiles of both the galaxy and the CGM.

The effect of the self-shielding model on different region of the halo is further illustrated in Figure 9, which shows the comparison between *EarlyRe-ray* and *EarlyRe-apx* with respect to the gas mass fraction and the H_2 fraction in four radial bins. We crossmatch and select halos whose gas is resolved enough for us to locate the baryonic center of mass and distinctly separate the halo into multiple bins. We end up with 26 halos, including halos without any stars, to calculate the statistics. The figure shows that while the gas mass fraction remains consistent between the two models across

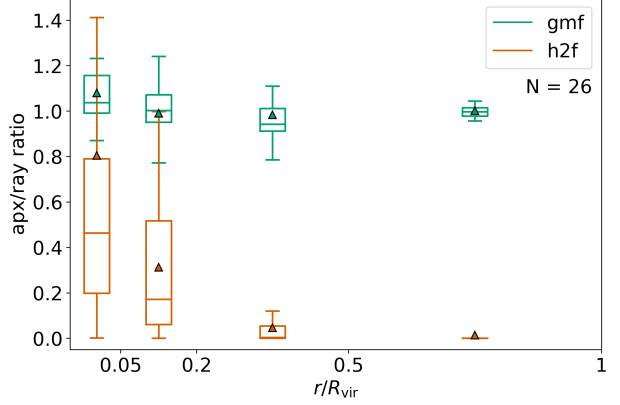


Figure 9. The comparison of the gas mass fraction (gmf) and H_2 fraction (h2f) in different radial bins (0 to $0.05 R_{\text{vir}}$, 0.05 to $0.2 R_{\text{vir}}$, 0.2 to $0.5 R_{\text{vir}}$, and 0.5 to $1 R_{\text{vir}}$) between the *EarlyRe-ray* and the *EarlyRe-apx* simulations at $z = 10.89$. The sample size for the statistics is 26 halos. The box represents the first and third quartile of the sample. The whiskers extend from the box to the further point within 1.5 times the inter-quartile range. The median is shown as a line in the box and the mean is shown as a triangle point.

all radial bins, the ratio of H_2 fraction between the approximation and the ray tracing model shows a declining trend towards larger ratio. The H_2 fraction in *EarlyRe-apx* agrees with *EarlyRe-ray* only in the inner most region of the galaxy ($r < 0.05 R_{\text{vir}}$) where gas is at high density and thus the self-shielding factor is accurately calculated by the approximation model. As we go to the outer radius, gas density decreases and thus H_2 in *EarlyRe-apx* is under-shielded, leading to a decrease in the ratio of H_2 fraction. Further into the CGM ($r > 0.2 R_{\text{vir}} \approx R_{\text{bary},2000}$), the approximation model fails to estimate the self-shielding factor, leading to a clear absence of molecular hydrogen in this region when compared with the ray-tracing model.

It is important to note that we have an outlier in Figure 9 where a halo with mass $M_{\text{halo}} = 3.6 \times 10^{10} M_{\odot}$ has a H_2 fraction within $0.05 R_{\text{vir}}$ about 8 times larger in *EarlyRe-apx* compared to *EarlyRe-ray*. To ensure the readability of the figure, we exclude this outlier from the figure; however, you can still see its effect on pulling the mean value away from the median value. The reason for this big difference is because for this particular halo, the gas in the inner region is much more compact and reaches a higher density in *EarlyRe-apx*. In particular, the densest gas cell in the *EarlyRe-apx*'s halo is about 10^{-19} g/cm^3 , 10 times higher than the *EarlyRe-ray*'s counterpart. At $\rho_{\text{gas}} \approx 10^{-19} \text{ g/cm}^3$, according to Figure 1, the Sobolev-like approximation typically overestimate the self-shielding amount, leading to more H_2 being able to form. More H_2 forming corresponds to

more cooling, leading to the collapse of gas and increase in gas density. This results in a runaway effect that causes this halo to have noticeably high amount of H_2 in its inner region when using the approximation model. However, this halo is the only case where the H_2 fraction is considerably higher when using the approximation and it only happens near the galactic center. In most of the cases, this runaway effect only happens locally at a few dense gas cells (as also shown in the H_2 clumps in Figures 5 and 6) that it does not change the average H_2 fraction of the whole galactic region.

3.4. Effect on the large-scale universe and reionization

We extend our analysis to the whole simulation box to investigate the effect of H_2 self-shielding modeling on a large-scale universe. Figure 10 shows the projection plots at different snapshots within the simulation's refined region, which is about 1/10000 volume of the whole simulation box. While the large-scale structure of gas is similar between two simulations, the distribution of other properties differ greatly. The amount of molecular hydrogen in the ISM is much lower when using the Sobolev-like approximation method, especially after stars start to form in the simulation. Newly formed stars produce LW radiation that propagate the whole simulation's refined region and destroy H_2 in the low gas density region where the approximation model under-predicts the amount of shielding. The lowest H_2 density in the ISM of *EarlyRe-apx* is less than 10^{-36} g/cm^3 , while the H_2 density in the most diffuse region of *EarlyRe-ray* is nearly 10 dex higher. As the simulation progresses, H_2 is recreated surrounding the supernova's superbubbles and the galactic filaments. As we can see in the temperature projection plot, supernova explosions heat up and ionize the surrounding gas. The electron and proton created from the ionization provide ingredients for H_2 to form (Galli & Palla 1998, see Table 1). However, near the supernova explosion when the temperature becomes too hot, H_2 can then be destroyed via collisional mechanism. These explains the accumulation of H_2 around galaxies and galactic filaments and the temporary absence of H_2 close to galaxies after stellar feedback in Figure 10. At high gas density region inside galaxies, H_2 can form via a three-body interaction between three atomic hydrogen (Palla et al. 1983) or via grain catalysis (Gould & Salpeter 1963).

As pointed out in Section 3.2, galaxies in *EarlyRe-ray* experience more prolonged star forming period than their counterparts in *EarlyRe-apx* and thus more metals are pushed out simultaneously in each period. This leaves shorter time for pristine gas to mix in to reduce the gas metallicity. Furthermore, more metals being

produced at once helps contaminate the IGM more easily. When metals get out to the IGM, because of the medium's very low gas density for mixing, metallicity does not decrease over time, creating more extended metal-rich regions spanning out to the IGM in the ray-tracing simulation. It is important to note that this difference in metallicity originates from the difference in star formation history rather than the amount of metals being produced because the galaxies in two simulations have relatively similar stellar mass and total supernova energy, as shown in Figure 5.

As suggested by Figure 10, the universe in *EarlyRe-apx* is much hotter at $z \approx 10.9$ than its counterpart in *EarlyRe-ray*. Because cosmic reionization is linked to the heating of the IGM (D'Aloisio et al. 2019), we expect that reionization is affected by the choice of self-shielding modeling. Figure 11 shows the distribution of neutral hydrogen fraction χ_{HI} within the refined region between our two simulations. The χ_{HI} value of 0 corresponds to complete ionization of atomic hydrogen. High-energy radiation from galaxies ionizes hydrogen, decreasing χ_{HI} in the surrounding IGM regions. χ_{HI} can go up again during recombination between protons and electrons to form neutral hydrogen, which is efficient at temperature lower than 10^4 K (Wise 2019). In all time steps shown, *EarlyRe-apx* displays more extended and prominent region of ionized hydrogen, expanding out to the further IGM region. On the other hand, hydrogen is less ionized in *EarlyRe-ray*, and ionized hydrogen is limited around the galaxy filament (shown in the top two rows of Figure 10). This observation is quantified in Figure 12 where we plot the volume-weighted average of χ_{HI} within the simulation's refined region as a function of time. At the start of both simulations, the universe is dominated with neutral hydrogen ($\chi_{\text{HI}} \approx 1$). However, about 0.32 Gyr after the Big Bang ($z \approx 13.5$), the volume-weighted average of the neutral hydrogen fraction starts to drop considerably in the approximation model when the ray-tracing model only shows a slight decline. By the end of the simulation, while more than 90% of hydrogen is still neutral in *EarlyRe-ray*, only about 65% of hydrogen remains as such in *EarlyRe-apx*. While both simulations are not run long enough to cover the whole reionization epoch, Figure 12 suggests that the reionization may be complete earlier in *EarlyRe-apx* than in *EarlyRe-ray*, even though the reionization's start time is similar. This illustrates that the use of Sobolev-like approximation to model H_2 self-shielding speeds up the reionization process and thus affect our theoretical prediction and modeling of the reionization epoch.

4. DISCUSSION AND CONCLUSION

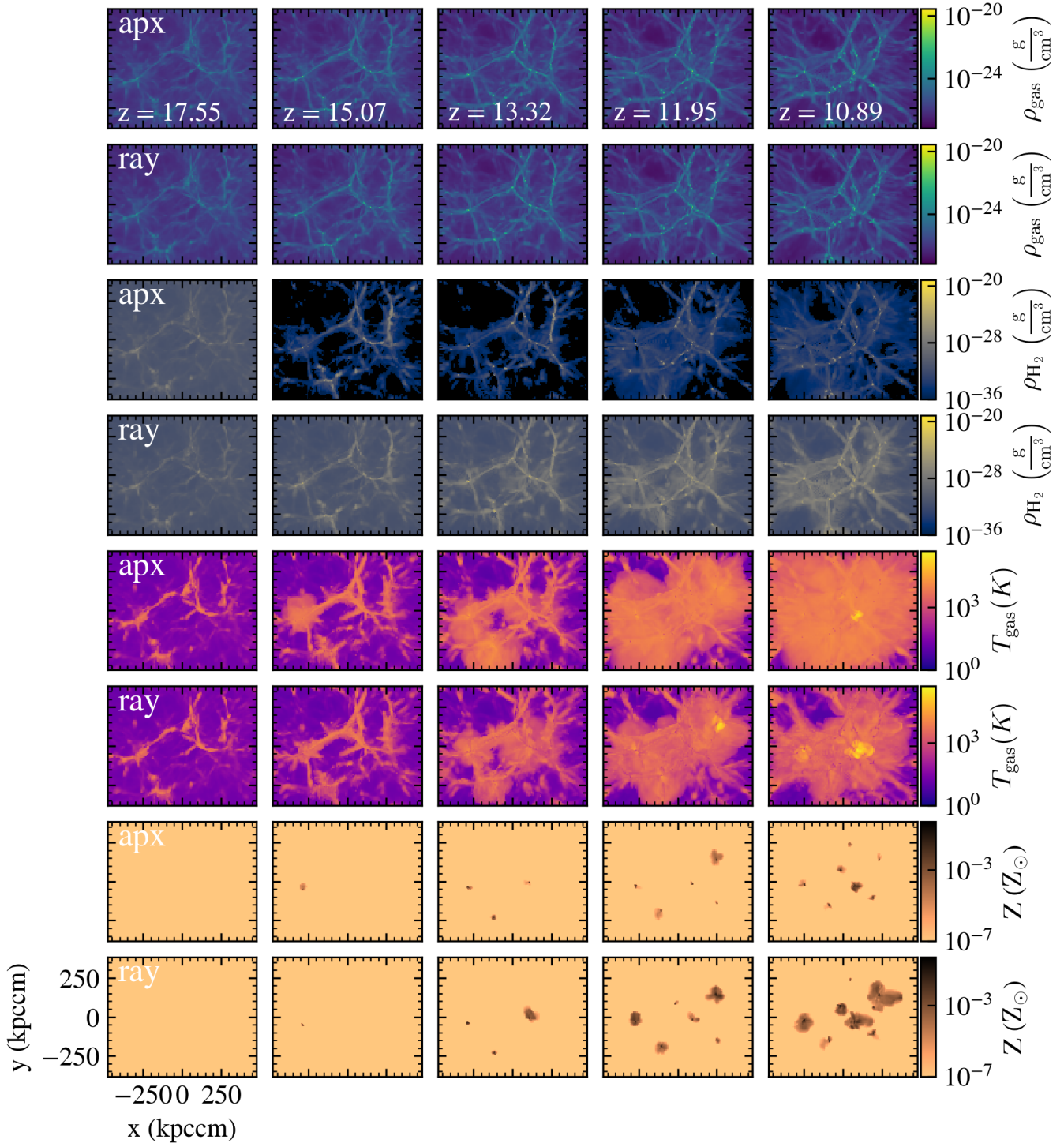


Figure 10. The gas density (1st and 2nd row), H_2 density (3rd and 4th row), gas temperature (5th and 6th row), and gas metallicity (7th and 8th row) within the simulation's refined region between the *EarlyRe-apx* and *EarlyRe-ray* across five time steps.

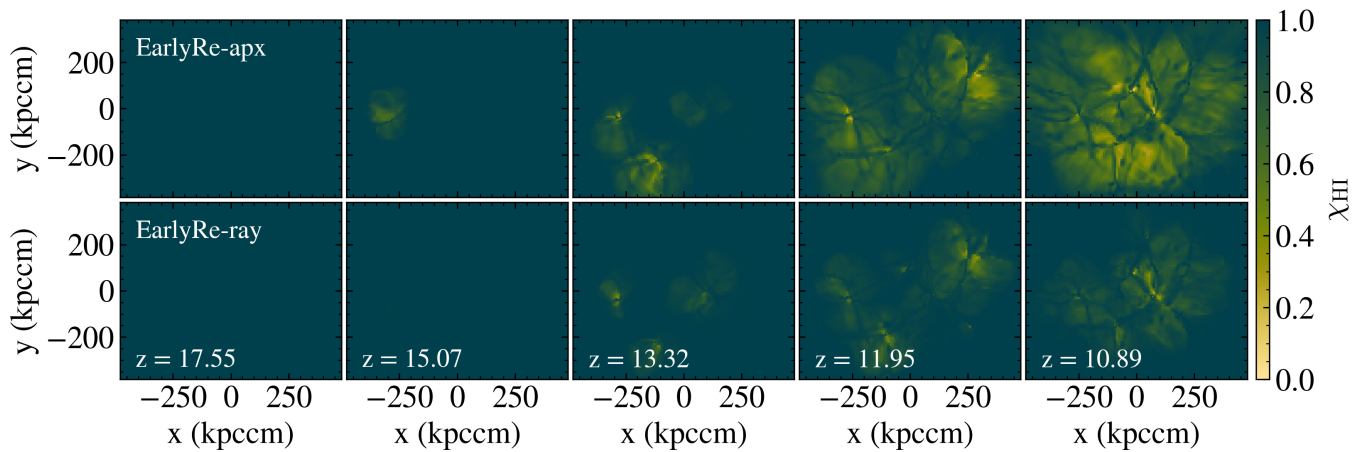


Figure 11. The neutral hydrogen fraction in the refined region box between the *EarlyRe-ray* and *EarlyRe-apx* simulations across five time steps.

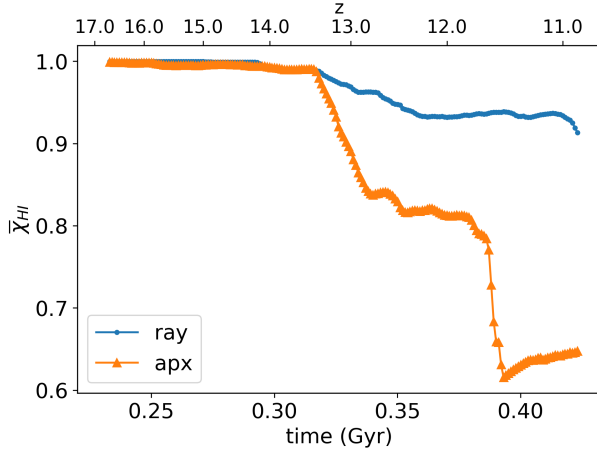


Figure 12. The comparison between the volume-weighted average of the neutral hydrogen fraction as a function of time between the *EarlyRe-ray* and the *EarlyRe-apx* simulations.

In this paper, using high-resolution zoom-in simulations, we run two radiative transfer models of molecular hydrogen self-shielding to examine their effect on galaxy evolution. The two models are the Sobolev-like approximation that uses local gas property to estimate the H_2 photodissociation rate and the ray tracing model based on HEALPix scheme. In summary, our key findings are as follows:

- The Sobolev-like approximation for H_2 self-shielding underestimates the self-shielding factor at low gas density ($\rho_{\text{gas}} \leq 10^{-22} \text{ g/cm}^3$) while overestimates the self-shielding factor at high gas density ($\rho_{\text{gas}} \geq 10^{-19} \text{ g/cm}^3$). This leads to halos in the simulation with the approximation model having their H_2 fraction several dex lower than their counterparts in the simulation with ray tracing model, especially for lower mass halo. (Figures 1 and 2)

- The Sobolev-like approximation affects star formation in cosmological simulation. Lower-mass halos ($M_{\text{halo}} < 10^9 M_{\odot}$) are harder to form stars due to the lack of molecular hydrogen fuel. Bigger halos are less affected and still converge in stellar mass between the two models. (Figures 3, 4)
- Even though there is convergence in the total stellar mass, the star formation history in the ray-tracing model shows more prolonged period of star formation while the approximation model shows a more bursty behavior. The different star formation behavior results in metals being produced, distributed, and mixed differently in the two simulation. This leads to a discrepancy in the metallicity and temperature profile between the two simulations where the ray-tracing model shows a more metal-riched and cooler ISM. (Figures 5, 6, and 10)
- Because the CGM is less dense than the galaxy, the effect of the approximation is more prominent in the outer region of the halo. Also, halos in the simulation with ray-tracing have more cool diffuse gas than in the simulation with the approximation model. (Figures 7, 8, and 9)
- The Sobolev-like approximation also effect the timing of the reionization epoch in cosmological simulation, where it make the universe reionize much quicker than the prediction using the ray tracing model. (Figures 11 and 12)

MORE DISCUSSION ON THE IMPACT OF THE STUDY.

Acknowledgement: We would like to thank [insert Grant number] and CAPS fellowship.

REFERENCES

- Abel, T., Wise, J. H., & Bryan, G. L. 2007, The Astrophysical Journal, 659, L87, doi: [10.1086/516820](https://doi.org/10.1086/516820)
- Bryan, G. L., Norman, M. L., O’Shea, B. W., et al. 2014, The Astrophysical Journal Supplement Series, 211, 19, doi: [10.1088/0067-0049/211/2/19](https://doi.org/10.1088/0067-0049/211/2/19)
- Chiaki, G., & Wise, J. H. 2023, Monthly Notices of the Royal Astronomical Society, 520, 5077, doi: [10.1093/mnras/stad433](https://doi.org/10.1093/mnras/stad433)
- Christensen, C., Quinn, T., Governato, F., et al. 2012, Monthly Notices of the Royal Astronomical Society, 425, 3058, doi: [10.1111/j.1365-2966.2012.21628.x](https://doi.org/10.1111/j.1365-2966.2012.21628.x)
- D’Aloisio, A., McQuinn, M., Maupin, O., et al. 2019, The Astrophysical Journal, 874, 154, doi: [10.3847/1538-4357/ab0d83](https://doi.org/10.3847/1538-4357/ab0d83)
- Davé, R. 2008, Monthly Notices of the Royal Astronomical Society, 385, 147, doi: [10.1111/j.1365-2966.2008.12866.x](https://doi.org/10.1111/j.1365-2966.2008.12866.x)
- Draine, B. T., & Bertoldi, F. 1996, The Astrophysical Journal, 468, 269, doi: [10.1086/177689](https://doi.org/10.1086/177689)

- 960 Field, G. B., Somerville, W. B., & Dressler, K. 1966,
 961 Annual Review of Astronomy and Astrophysics, 4, 207,
 962 doi: [10.1146/annurev.aa.04.090166.001231](https://doi.org/10.1146/annurev.aa.04.090166.001231)
- 963 Galli, D., & Palla, F. 1998, *Astronomy and Astrophysics*,
 964 335, 403, doi: [10.48550/arXiv.astro-ph/9803315](https://doi.org/10.48550/arXiv.astro-ph/9803315)
- 965 Glover, S. C. O., & Mac Low, M.-M. 2007a, *The
 966 Astrophysical Journal Supplement Series*, 169, 239,
 967 doi: [10.1086/512238](https://doi.org/10.1086/512238)
- 968 —. 2007b, *The Astrophysical Journal*, 659, 1317,
 969 doi: [10.1086/512227](https://doi.org/10.1086/512227)
- 970 Gnedin, N. Y., & Kravtsov, A. V. 2011, *The Astrophysical
 971 Journal*, 728, 88, doi: [10.1088/0004-637X/728/2/88](https://doi.org/10.1088/0004-637X/728/2/88)
- 972 Gnedin, N. Y., Tassis, K., & Kravtsov, A. V. 2009, *The
 973 Astrophysical Journal*, 697, 55,
 974 doi: [10.1088/0004-637X/697/1/55](https://doi.org/10.1088/0004-637X/697/1/55)
- 975 Gorski, K. M., Hivon, E., Banday, A. J., et al. 2005, *The
 976 Astrophysical Journal*, 622, 759, doi: [10.1086/427976](https://doi.org/10.1086/427976)
- 977 Gould, R. J., & Salpeter, E. E. 1963, *The Astrophysical
 978 Journal*, 138, 393, doi: [10.1086/147654](https://doi.org/10.1086/147654)
- 979 Greif, T. H. 2014, *Monthly Notices of the Royal
 980 Astronomical Society*, 444, 1566,
 981 doi: [10.1093/mnras/stu1532](https://doi.org/10.1093/mnras/stu1532)
- 982 Hartwig, T., Clark, P. C., Glover, S. C. O., Klessen, R. S.,
 983 & Sasaki, M. 2015a, *The Astrophysical Journal*, 799, 114,
 984 doi: [10.1088/0004-637X/799/2/114](https://doi.org/10.1088/0004-637X/799/2/114)
- 985 Hartwig, T., Glover, S. C. O., Klessen, R. S., Latif, M. A.,
 986 & Volonteri, M. 2015b, *Monthly Notices of the Royal
 987 Astronomical Society*, 452, 1233,
 988 doi: [10.1093/mnras/stv1368](https://doi.org/10.1093/mnras/stv1368)
- 989 Johnson, J. L., Khochfar, S., Greif, T. H., & Durier, F.
 990 2011, *Monthly Notices of the Royal Astronomical Society*,
 991 410, 919, doi: [10.1111/j.1365-2966.2010.17491.x](https://doi.org/10.1111/j.1365-2966.2010.17491.x)
- 992 Kannan, R., Macciò, A. V., Fontanot, F., et al. 2015,
 993 *Monthly Notices of the Royal Astronomical Society*, 452,
 994 4347, doi: [10.1093/mnras/stv1633](https://doi.org/10.1093/mnras/stv1633)
- 995 Kennicutt, R. C. 1998, *Annual Review of Astronomy &
 996 Astrophysics*, 36, 189,
 997 doi: [10.1146/annurev.astro.36.1.189](https://doi.org/10.1146/annurev.astro.36.1.189)
- 998 Kennicutt, R. C. J., Calzetti, D., Walter, F., et al. 2007,
 999 *The Astrophysical Journal*, 671, 333, doi: [10.1086/522300](https://doi.org/10.1086/522300)
- 1000 Leroy, A. K., Walter, F., Sandstrom, K., et al. 2013, *The
 1001 Astronomical Journal*, 146, 19,
 1002 doi: [10.1088/0004-6256/146/2/19](https://doi.org/10.1088/0004-6256/146/2/19)
- 1003 Palla, F., Salpeter, E. E., & Stahler, S. W. 1983, *The
 1004 Astrophysical Journal*, 271, 632, doi: [10.1086/161231](https://doi.org/10.1086/161231)
- 1005 Planck Collaboration, Ade, P. A. R., Aghanim, N., et al.
 1006 2016, *Astronomy and Astrophysics*, 594, A13,
 1007 doi: [10.1051/0004-6361/201525830](https://doi.org/10.1051/0004-6361/201525830)
- 1008 Safranek-Shrader, C., Krumholz, M. R., Kim, C.-G., et al.
 1009 2017, *Monthly Notices of the Royal Astronomical Society*,
 1010 465, 885, doi: [10.1093/mnras/stw2647](https://doi.org/10.1093/mnras/stw2647)
- 1011 Schmidt, M. 1959, *The Astrophysical Journal*, 129, 243,
 1012 doi: [10.1086/146614](https://doi.org/10.1086/146614)
- 1013 Shang, C., Bryan, G. L., & Haiman, Z. 2010, *Monthly
 1014 Notices of the Royal Astronomical Society*, 402, 1249,
 1015 doi: [10.1111/j.1365-2966.2009.15960.x](https://doi.org/10.1111/j.1365-2966.2009.15960.x)
- 1016 Sobolev, V. V. 1957, *Soviet Astronomy*, 1, 678
- 1017 Stecher, T. P., & Williams, D. A. 1967, *The Astrophysical
 1018 Journal*, 149, L29, doi: [10.1086/180047](https://doi.org/10.1086/180047)
- 1019 Stevens, A. R. H., Martig, M., Croton, D. J., & Feng, Y.
 1020 2014, *Monthly Notices of the Royal Astronomical Society*,
 1021 445, 239, doi: [10.1093/mnras/stu1724](https://doi.org/10.1093/mnras/stu1724)
- 1022 Thoul, A. A., & Weinberg, D. H. 1995, *The Astrophysical
 1023 Journal*, 442, 480, doi: [10.1086/175455](https://doi.org/10.1086/175455)
- 1024 Wise, J. H. 2019, *Contemporary Physics*, 60, 145,
 1025 doi: [10.1080/00107514.2019.1631548](https://doi.org/10.1080/00107514.2019.1631548)
- 1026 Wise, J. H., & Abel, T. 2011, *Monthly Notices of the Royal
 1027 Astronomical Society*, 414, 3458,
 1028 doi: [10.1111/j.1365-2966.2011.18646.x](https://doi.org/10.1111/j.1365-2966.2011.18646.x)
- 1029 Wise, J. H., & Cen, R. 2009, *The Astrophysical Journal*,
 1030 693, 984, doi: [10.1088/0004-637X/693/1/984](https://doi.org/10.1088/0004-637X/693/1/984)
- 1031 Wolcott-Green, J., Haiman, Z., & Bryan, G. L. 2011,
 1032 *Monthly Notices of the Royal Astronomical Society*, 418,
 1033 838, doi: [10.1111/j.1365-2966.2011.19538.x](https://doi.org/10.1111/j.1365-2966.2011.19538.x)
- 1034 Wong, T., & Blitz, L. 2002, *The Astrophysical Journal*,
 1035 569, 157, doi: [10.1086/339287](https://doi.org/10.1086/339287)
- 1036 Yoshida, N., Abel, T., Hernquist, L., & Sugiyama, N. 2003,
 1037 *The Astrophysical Journal*, 592, 645, doi: [10.1086/375810](https://doi.org/10.1086/375810)
- 1038 Yoshida, N., Oh, S. P., Kitayama, T., & Hernquist, L. 2007,
 1039 *The Astrophysical Journal*, 663, 687, doi: [10.1086/518227](https://doi.org/10.1086/518227)
- 1040 Yoshida, N., Omukai, K., Hernquist, L., & Abel, T. 2006,
 1041 *The Astrophysical Journal*, 652, 6, doi: [10.1086/507978](https://doi.org/10.1086/507978)